RESEARCH

Experimental and Analytical Investigation of Deflection of R-UHPFRC Beams Subjected to Loading–Unloading

Bartłomiej Sawicki[1,2*] and Eugen Brühwiler[1]

Abstract

Under service conditions, R-UHPFRC (Reinforced Ultra High Performance Fiber Reinforced Cementitious composite) beams exhibit residual deflection after loading–unloading. This is due to the tensile strain hardening behavior of UHPFRC. The precise calculation of deflection is thus relevant and was not addressed previously. This paper proposes a material model for UHPFRC under loading–unloading and a numerical layered model for the calculation of stress and strain distribution in the cross section. Then, a curvature-based analytical model is presented for calculation of deflection of a beam. This method is finally compared and validated against experimental results as obtained from four-point bending of full-scale R-UHPFRC beams. This research reveals the need for a specific material model for UHPFRC subjected to loading–unloading for the precise calculation of the structural response of elements and members under repetitive loading, such as service or fatigue loading.

Keywords Cement-based composites, Fibers, UHPFRC, Deflection, Design, Beams, Modelling, Analytical, Experiments

1 Introduction

UHPFRC (Ultra High Performance Fiber Reinforced Cementitious composite) is a structural material made of cementitious matrix with fine grains (< 1 mm) and short straight steel fibers in high dosage (> 3% vol.) (Brühwiler, 2016). UHPFRC is often combined with steel reinforcement bars in the direction of main stress, forming R-UHPFRC (reinforced UHPFRC). Thanks to its durability, versatility and structural potential (Graybeal et al., 2020), the number of UHPFRC applications for the rehabilitation and strengthening of existing structures as well

as for the design and construction of new structures is growing rapidly in Switzerland (Bertola et al., 2021; EPFL, 2023) and around the world (Azmee & Shafiq, 2018; Yoo & Yoon, 2016).

Majority of researchers and designers focus on the ultimate resistance and deflection (Khorami et al., 2021; Sadaghian et al., 2021; Shen et al., 2020; Yoo et al., 2016) of UHPFRC elements and structures under monotonic loading. Lately, while investigating fatigue mechanism of R-UHPFRC beams, strain and crack opening variation was analyzed in subsequent loading–unloading cycles (Sawicki 2021). It was observed that the strain profile of unloaded beams changes radically after the first cycle due to creation of microcracks and their residual opening. It was then deduced and proven that the residual opening of microcracks produces a complex stress distribution, with compressive stresses activated in the bottom of a beam even under the sagging bending moment, where the tensile stress would be expected (Sawicki et al., 2022).

The goal of this paper is to analyze the residual deflection, or a difference between deflection at loaded and

*Correspondence:
Bartłomiej Sawicki
bartek.sawicki@alumni.epfl.ch
[1] Laboratory for Maintenance and Safety of Structures (MCS), Civil Engineering Institute, Swiss Federal Institute of Technology Lausanne (EPFL), EPFL ENAC IIC MCS, Station 18, CH-1015 Lausanne, Switzerland
[2] Institute of Structural Design (ITE), Faculty of Architecture, Civil Engineering and Environmental Sciences, Technische Universität Braunschweig, Pockelsstrasse 4, DE-38106 Braunschweig, Germany

unloaded (or partially unloaded) states, of R-UHPFRC beams subjected to loading–unloading as it occurs due to traffic and other repetitive loading. The precise calculation of relative deflection is important e.g. in case of railway bridges. A simple analytical method for calculation is proposed and compared with experimental results of R-UHPFRC beams that have been loaded-unloaded at various stages. A simple material model, based on testing of accompanying small-scale specimens of UHPFRC, is used for this verification.

2 Literature Review on Modelling of UHPFRC

Due to its composite constitution, UHPFRC presents bi-linear response under tensile stress with elastic and strain-hardening stages (Naaman, 2018) until reaching the tensile strength, followed by strain-softening. This relatively complex material behavior makes modelling of structures a nontrivial task (Sadaghian et al., 2021) requiring nonlinear solvers. Nevertheless, several analytical and numerical methods for calculation of area moment of inertia and deflection of R-UHPFRC beams were presented already.

An analytical solution for the calculation of the area moment of inertia of R-UHPFRC beams with part of material in the strain-hardening domain was proposed in Yoo et al. (2016). The tensile stress area with bi-linear stress distribution is replaced with a fictitious equivalent elastic stress block, of smaller height and an effective elasticity modulus based on proportionality of stress and strain at the bottom of the block. The calculated deflection using the modified ACI 440.1R 15 method (Bischoff model) (ACI Committee, 2015) matched well results of three-point-bending experiments up to the strain at the bottom of the beam reaching around two-thirds of the strain corresponding to the ultimate tensile strength strain of UHPFRC (ε_u). After this point, the obtained beam response was overly stiff. Since the test was performed under three-point-bending, the contribution to the global beam response of the section with lower moment of inertia due to strain-hardening was relatively small compared with four-point bending tests. Furthermore, the strain-hardening of the tested UHP-FRC was not very pronounced compared with the elastic part facilitating the calculation, with an elastic limit stress $f_e = 12.5$ MPa and a tensile strength $f_u = 14.3$ MPa. The authors did not consider unloading–reloading of the beam.

Another method for calculation of the effective area moment of inertia using similar principles as for cracked reinforced concrete beams was presented in Gao et al., 2020. To calculate the area moment of inertia, fibers are considered separately and treated as reinforcement uniformly distributed over the height of an element while the tensile stress contribution of the cementitious matrix is neglected. The authors did not compare the calculated deflection with experimental results, and for validation, the obtained area moment of inertia was used for the calculation of stress distribution in the cross section of the structural element subjected to static and fatigue loading.

Closed-form analytical solutions for calculating deflection of beams and slabs under various loadings and assuming bi-linear moment–curvature relationship of cross-section were developed in Wang (2015). By means of a parametrized constitutive law of UHPFRC (Soranakom & Mobasher, 2007), bending moment–deflection curves were calculated, reflecting well the structural response of a beam. However, the assumed linearity of moment–curvature holds as long as the tensile strength of UHPFRC is not reached. Depending on the shape and proportions of cross-sections, this can be achieved before the ultimate resistance of the structural element is attained (Denarié et al., 2017; Sawicki & Brühwiler, 2019; Sawicki et al., 2022). The unloading–reloading stiffness of the beam was not considered by the authors.

A layered numerical model was used for calculation of the moment–curvature relationship of beams made of non-strain-hardening fiber reinforced cementitious material (Yang et al., 2019). The curvature was calculated on the basis of the strain profile and stress distribution leading to the sectional force equilibrium.

An approach with Bischoff method, bi-linear curvature distribution and layered model was used by Peng et al. (2022), and verified with experiments available in literature. Using statistical methods, they have found a good agreement in particular at service loading, i.e. around half of the beam resistance. They have also found that the calculation on the basis of direct beam integration and use of layered model for calculation of curvature leads to a more precise solution. No unloading–reloading cycles were considered.

3 Experimental Investigation

The experiments presented hereby were originally designed for fatigue testing (Sawicki & Brühwiler, 2019). Using the same batch, T-shaped beams and small plates for material testing were cast. Before fatigue testing, each beam was quasi-statically pre-loaded and unloaded to various load levels. The experimental setup and results are presented below. The results of beam testing in terms of deflection vs. load curves are presented later, alongside with modelling results.

3.1 Setup

Three types of beams with T-cross section were tested: Type I with a single Ø20 mm steel rebar; Type II with a single Ø34 mm rebar and Type III with Ø20 mm

longitudinal rebar and Ø6 mm Ω shaped stirrups. Their dimensions are specified in Fig. 1. The beams were casted in horizontal position (as tested), pouring the fresh UHPFRC from top at one end. Six external vibrators were used to assure good flow of the fresh UHPFRC. These beams, and their sectional dimensions, represent well a typical design of R-UHPFRC beams(Brühwiler et al., 2019) and thus allow for verification of the proposed methodology in view of structural applications.

All beams were tested under four-point bending at least 90 days after production. The reference deflection was measured after positioning of the beams on the testing rig, therefore under self-weight. Loading was applied using one servo-hydraulic actuator and a steel redistribution beam of high stiffness. The load application points were positioned symmetrically, and their spacing *b* is indicated in Fig. 1. The spacing varied to avoid shear failure in these relatively stiff test setups. For all the beams, the vertical displacement at mid-span and over
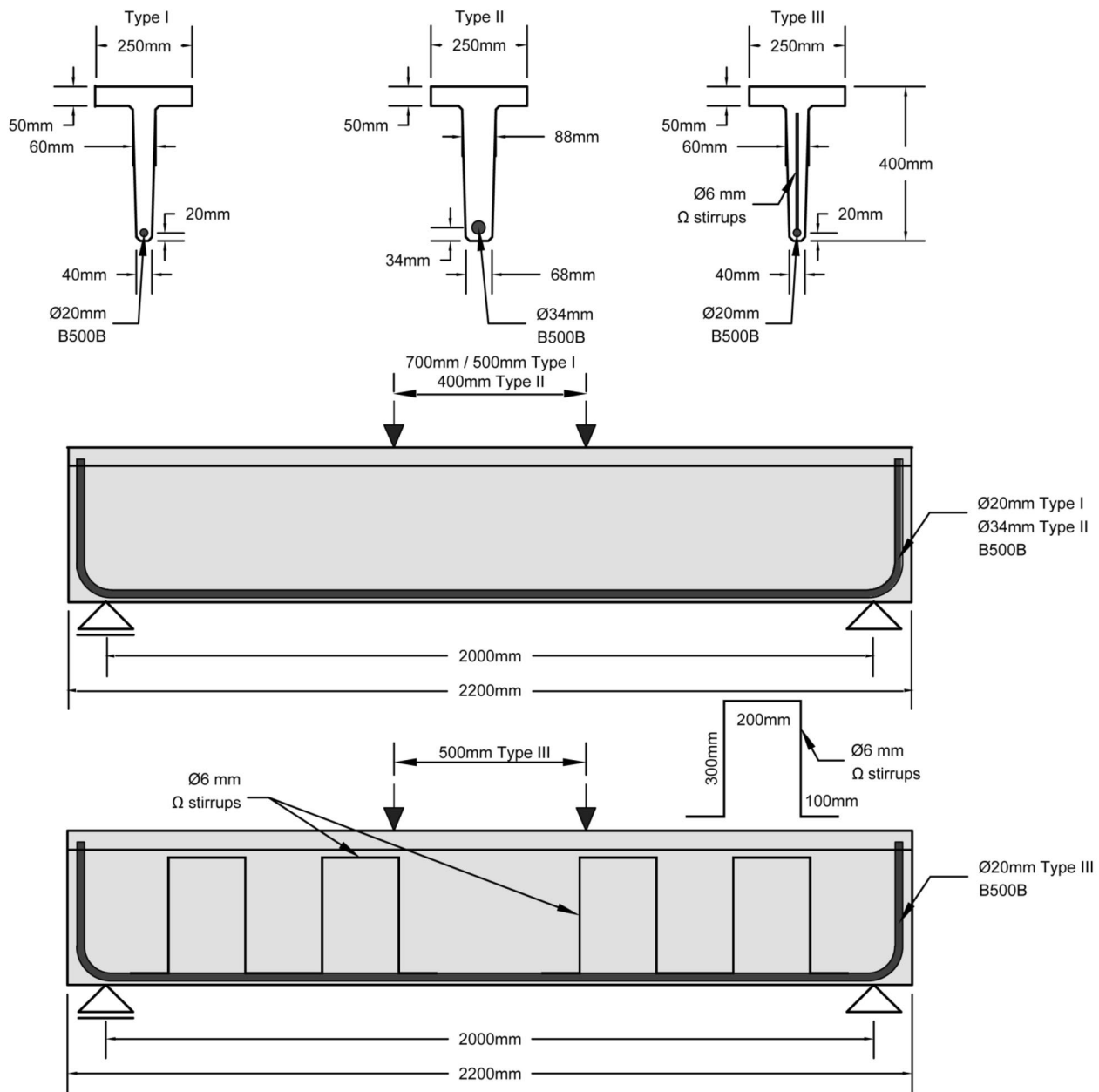

Fig. 1 Scheme of beams under testing

Table 1 Mean tensile material properties of UHPFRC based on inverse analysis of beams

Beam type	f_e [MPa]	f_u [MPa]	ε_u [‰]	E_U [GPa]
Type I (Ø20 mm)	6.3	12.0	3.5	43.1
Type II (Ø34 mm)	4.9	10.9	3.7	41.1
Type III (Ø20 mm)	4.4	11.8	3.0	36.1

Table 2 Mean tensile material properties of reinforcement bars based on axial tensile tests

Beam type	f_s [MPa]	f_t [MPa]	ε_u [%]
Type I (Ø20 mm)	600	687	9.2
Type II (Ø34 mm)	525	624	9.4
Type III (Ø20 mm)	512	617	9.2

the supports was measured using LVDTs. The deflection of beams is corrected with vertical displacement over the supports.

3.2 Materials

Commercially available UHPFRC mix Holcim710®, with 3.8% in volume of 13 mm long straight steel fibres with an aspect ratio of 65, was used to fabricate the beams. The tensile material properties were retrieved for each type of beam using 30 mm thin 4-point bending plates, as described in detail in Sawicki et al. (2022). The following properties were determined: (1) elastic limit stress f_e; (2) tensile strength f_u; (3) hardening strain at tensile strength ε_u; and (4) modulus of elasticity E_U. The results are given in Table 1.

Both longitudinal reinforcement and stirrups are of type B500B according to Eurocode (EC2. Eurocode, 2005), with nominal characteristic yield stress $f_{sk} = 500$ MPa. The properties of steel reinforcement bars obtained from direct tension testing are presented in Table 2, where f_s stands for yielding stress, f_t for tensile strength, ε_u for rupture strain. The modulus of elasticity E_s is assumed as 205 GPa. The rebars used in Type I beams have higher strength; however, they still meet the requirements of B500B reinforcement class.

The longitudinal reinforcement bars in Type I and Type III beams are of the same diameter and class, but were fabricated by different producers and thus their properties vary. Furthermore, material tests revealed the tensile response of UHPFRC in Type III beams is different than expected due to casting one year later than the other specimens. Therefore, Type I and Type III beams are treated separately.

4 Modelling

4.1 Calculation of Strain Distribution and Curvature

4.1.1 Material Model of UHPFRC

UHPFRC is a composite material made of a cementitious matrix and fibers. Due to this bi-component constitution, UHPFRC shows quasi bi-linear stress–strain behavior under direct tension before reaching its tensile strength. The tensile response of UHPFRC, with values typical for material used in the current research, are presented in Fig. 2.

The first stage is elastic. The behavior of UHPFRC is linear with Young's modulus E_U and after unloading the strain comes back to zero. After the elasticity limit (f_e, ε_e, Fig. 2) is reached, uniformly distributed discontinuities in the matrix start to occur and the material enters the strain-hardening domain with strain-hardening secant E_{Uh}. From the macroscopic viewpoint, the material can be considered as a continuum, however increasingly anisotropic as hardening develops.

When UHPFRC is in the strain-hardening domain, after unloading the residual strain $\varepsilon_{res,i}$ remains. Subjected again to tension, the response follows E_{Ui} until the previously imposed stress is reached. If the tensile stress is further increased, the material follows the envelope strain-hardening curve shown in Fig. 2.

When the tensile strength is reached, the unloading secant modulus is calculated according to:

$$E_{Uu} = \frac{f_u}{k_u \cdot \varepsilon_u}, \tag{1}$$

where $k_u = 0.5$ for UHPFRC with straight steel fibers (Wille & Naaman, 2010).

It is assumed that the unloading secant E_{Ui} varies linearly from E_U to E_{Uu} between ε_e and ε_u respectively (see Fig. 2), which is in agreement with the behavior of fiber reinforced mortar at the onset of matrix cracking (Visalvanich & Naaman, 1981). Due to the residual strain ε_{res} accumulated in the material after unloading, the internal force balance can lead to such a distribution of strain in the member that the material at the bottom of the beam enters into compression (Sawicki et al., 2022). To the authors' knowledge, there was no study on the behavior of UHPFRC in compression after previously reaching the strain-hardening domain in tension. Tensile strain-hardening cement-based composites with steel fibers seem to follow the unloading secant modulus E_{Ui} at the first stage of compressive response (Müller & Mechtcherine, 2016), and this is adopted in the present work.

Once the tensile strength f_u is reached, the softening stage begins. The stress can be assumed to decrease linearly until the formed crack opening w reaches half of the length of fiber (Fig. 2). For the current material $w_u = 6.5$ mm. Due to the dependence of non-dimensional
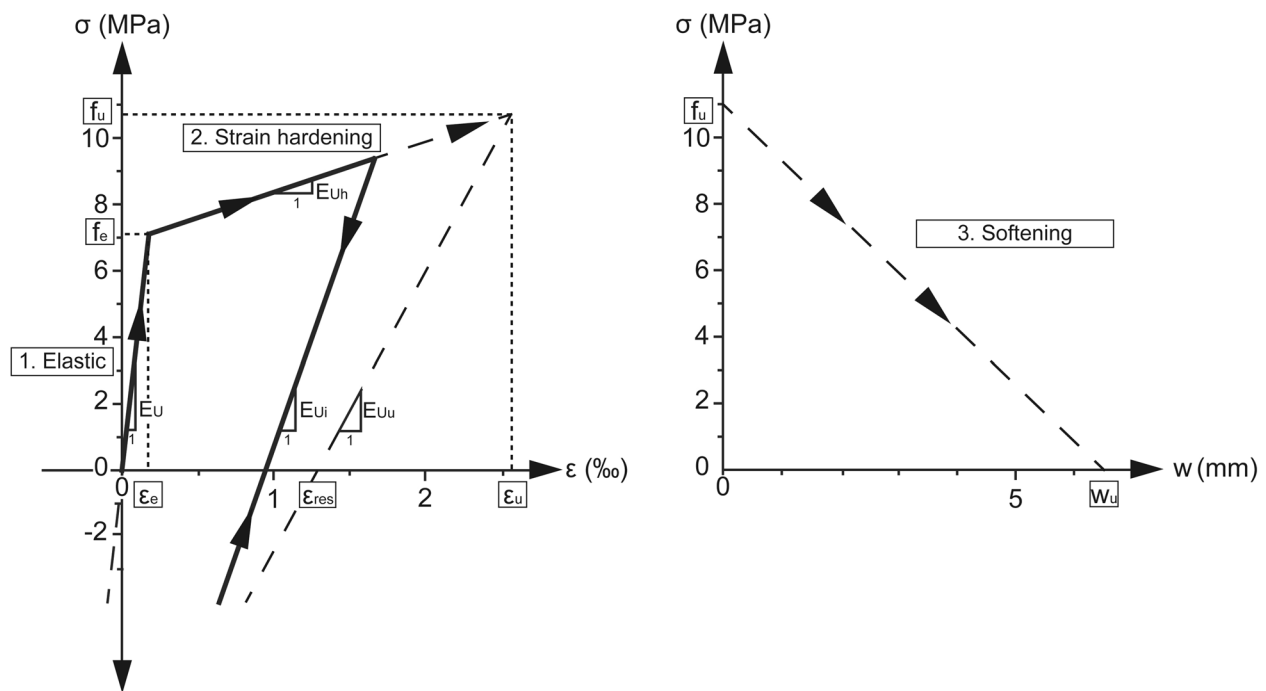
Fig. 2 Simplified UHPFRC constitutive tensile law; left: elasting and hardening regimes with unloding-reloading behaviour; right: post-peak softening

strain on the reference length (e.g. gauge length), it is assumed that the stress is reduced linearly until a deformation equal to 50% strain is reached in the layered model (crack of half of fiber length with reference of fiber length). This simplification is possible as only a small part of UHPFRC reaches strains larger than ε_u at the ultimate bending moment, and the post-peak structural behavior of the beam is not considered here.

It is assumed that the UHPFRC in compression, without pre-loading in tension, behaves linear-elastically with E_U up to the compressive strength f_{Uc}.

4.1.2 Numerical Model

The stress distribution in the cross section of the R-UHP-FRC beam is computed using Euler–Bernoulli elastic beam theory and numerical methods. Perfect bond between reinforcement bar and UHPFRC is assumed (Oesterlee, 2010).

The UHPFRC cross-section of the beam is discretized into 100 horizontal layers of equal thickness with uniform strain at each layer, as presented in Fig. 3. The elastic–strain-hardening–softening material model in tension and perfectly elastic model in compression is adopted for UHPFRC, as explained previously and shown in Fig. 2. The reinforcement bar is taken as the constant stress and strain layer, with elastic—perfectly plastic material model, which is valid for strains up to 2% as confirmed

by the direct tensile tests on reinforcement bars used in the experiments. Once the rupture strain ε_u is attained in the rebar, the stress is taken as zero. The area of UHPFRC is corrected with respect to the rebar area, assuming an equivalent constant strain and stress element being subtracted from the section with strain equal to the rebar's strain and material law of UHPFRC.

The linear strain distribution is governed by the strain ε_b at the bottom of the member's section and by the position of the neutral axis $x_{n\text{-}n}$ extending from the bottom. For given $x_{n\text{-}n}$, strain distribution in the UHPFRC and rebar is calculated. Based on the material law, stress in each layer and in the rebar is obtained. Resultant forces are computed respecting the beam geometry. The neutral axis $x_{n\text{-}n}$ is finally found stating force equilibrium when the sum of sectional forces $\sum F = 0$. Then, the resulting bending moment for the corresponding ε_b is calculated. The procedure is automated in such a way that for a given bending moment the unique pair of ε_b and $x_{n\text{-}n}$ is found, and thus the distribution of stress and strain in the cross section is determined. The corresponding bending moment M and curvature ϕ for the given stress and strain distribution is then calculated:

$$M = \sum \sigma_i \cdot t_i \cdot w_i \cdot (x_{n-n} - x_i), \tag{2}$$
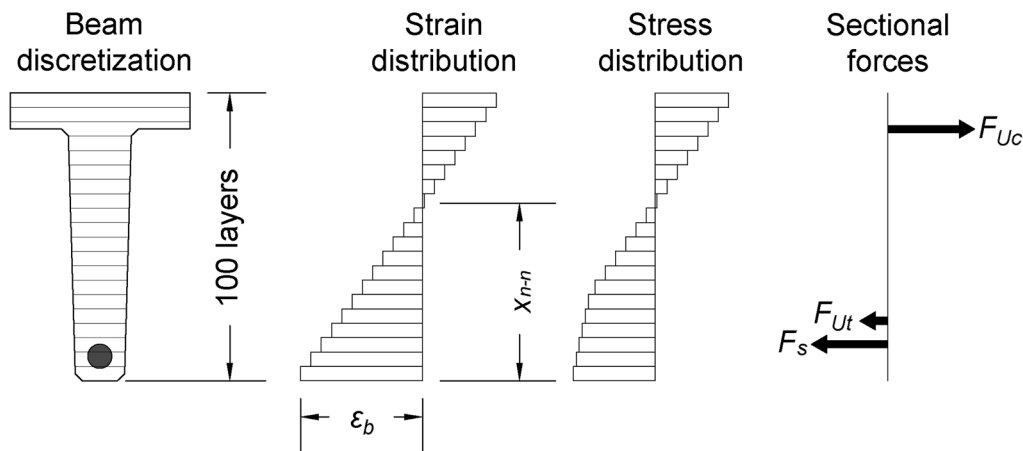
Fig. 3 Scheme of numerical model for calculation of stress and strain distribution under given bending moment; x_{n-n}—neutral axis position, F_{Uc}—compressive resultant force of UHPFRC, F_{Ut}—tensile resultant force of UHPFRC, F_s—resultant force of rebar

$$\varphi = \frac{\varepsilon_b}{x_{n-n}}, \tag{3}$$

where σ_i, t_i, w_i and x_i are respectively stress, thickness, width and position of ith layer of computational model.

To calculate the curvature during unloading, under lower bending moment M_{min}, the strain distribution needs to be determined once more. Using the previously obtained stress distribution under upper bending moment M_{max}, the unloading secants E_{Ui} and residual strains $\varepsilon_{res,i}$ are computed and stored for each UHPFRC layer using the relationship presented in Fig. 2. To find the strain distribution at M_{min}, a new pair of ε_b and x_{n-n} is found. The UHPFRC layers that entered the strain-hardening domain at M_{max} follow the unloading secant modulus E_{Ui} stored previously. Importantly, if in any layer the obtained strain is such that $0 < \varepsilon < \varepsilon_{res,i}$, the stress in the UHPFRC is negative (i.e. compressive stress) despite a positive strain value (see Fig. 2) (Sawicki et al., 2022). Previous research (Makita & Brühwiler, 2014; Oesterlee, 2010; Sawicki & Brühwiler, 2019) showed that the bond between UHPFRC and rebars is close to perfect. Furthermore, the strain distribution of UHPFRC along an element is highly irregular and the plastic deformation of steel reinforcement bars occurs mostly in the critical cross-section after UHPFRC discontinuity localization. Therefore, in the model, the stress–strain constitutive law of rebar at unloading follows the loading path, thus no residual deformation of rebar is considered. Having obtained the new strain distribution, M_{min} is calculated using Eq. (2) and curvature ϕ_{min} using Eq. (3).

4.2 Analytical Calculation of Deflection
During loading–unloading of a R-UHPFRC beam, three stages can be differentiated: (I) elastic; (II) hardening;

(III) unloading. During monotonic loading (stages I and II), the bending moment–curvature relationship can be approximated as bi-linear (Soranakom & Mobasher, 2007), with change of linearity at the elastic bending moment M_{El} (Fig. 4), after which part of UHPFRC material enters the strain hardening regime. This bi-linear relationship holds if the softening behavior in the critical section of the beam is ignored, and leads to distribution of curvature in the simply supported beam at stage II as presented in Fig. 5. The curvature distribution at stage III) unloading was not verified before to the authors'
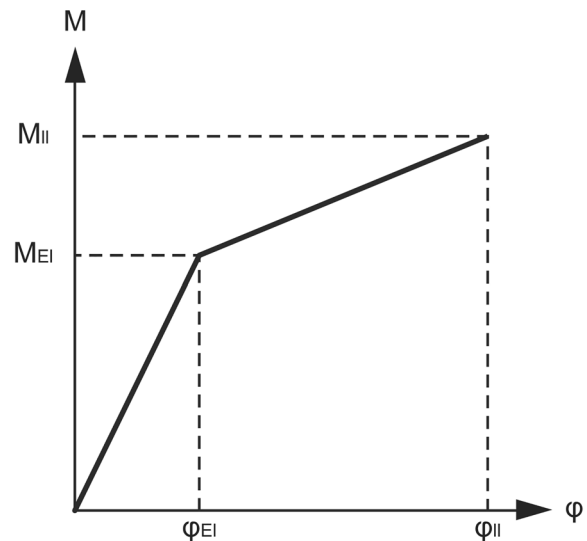

Fig. 4 Bi-linear moment–curvature relationship; M_{El} is the bending moment at limit of elasticity, and M_{II} is the bending moment above which bi-linearity holds no more, φ_{El} and φ_{II} are the respective curvatures
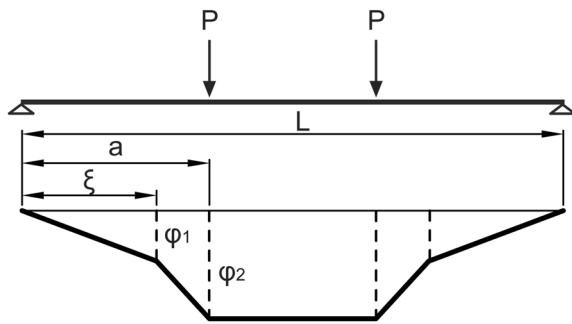
Fig. 5 Curvature distribution of beam under four-point bending with bi-linear moment–curvature

knowledge. Since the UHPFRC at unloading is following a different stress–strain path than under monotonic loading (Fig. 2), the curvature distribution in the beam is investigated in detail in Sect. 5.1.2. Because the distribution of strain in a beam is non-uniform due to microcracking of UHPFRC, and as deformation accumulation occurs in the critical section (ACI Committee, 2015), the rebar yields predominantly in the critical cross-section. Therefore, the plastic residual deformation of the rebar is not considered at the unloading stage.

At the elastic stage (I), stress in UHPFRC at all sections of a beam is below the limit of elasticity and thus the bending moment is below the elastic limit bending moment ($M_{max} < M_{El}$). Therefore, the stiffness is uniform along the beam and the classical formula from elasticity theory for calculation of deflection at mid-span can be used:

$$\delta_{max,el} = \frac{\varphi}{24}\left(3L^2 - 4a^2\right), \tag{4}$$

where ϕ is the curvature under the applied bending moment (and $\phi \le \phi_{El}$, see Fig. 4), L is the span of beam and a is the distance between support and force application point, as presented in Fig. 5. The elastic limit bending moment (M_{El}) and curvature (ϕ_{El}) are obtained using Eqs. (2) and (3) such that $\varepsilon_b = \varepsilon_e$.

At the hardening stage (II), UHPFRC in certain regions of the beam enters into the hardening domain as the applied upper bending moment $M_{max} > M_{El}$. The stress distribution is found iteratively using the layered model, and the bending moment and curvature are then calculated using Eqs. (2) and (3). A bi-linearity of curvature occurs along the beam as presented in Fig. 5. The following holds at this stage: $\phi_1 = \phi_{El}$; $M(\xi) = M_{El}$ and $\phi_2 = \phi(M_{max})$, see Fig. 4. An equation for deflection of a beam can be found by direct integration of curvature using Euler–Bernoulli beam theory (Garcez & Silva Filho, 2009; Wang, 2015). The bi-linearity of the

moment–curvature relation of strain-hardening fiber reinforced cementitious material beam under monotonic loading was verified by Soranakom and Mobasher (2007). The following formula to calculate deflection at mid-span of a beam with bi-linear moment–curvature under four-point bending (Fig. 5) is used (Garcez & Silva Filho, 2009):

$$\delta_{max} = \frac{\varphi_2}{24}\left(3L^2 - 4a^2\right) + \frac{(\xi + a)}{6}(\varphi_1 \cdot a - \varphi_2 \cdot \xi). \tag{5}$$

At the end of stage II, when the ultimate resistance bending moment M_{Rd} is achieved, part of UHPFRC can enter the softening regime with strain values larger than ε_u. The cross section height in the softening regime depends on the element's geometry (Denarié et al., 2017; Shen et al., 2020). It happens solely in the critical section where the localized crack is being formed (Sawicki & Brühwiler, 2019), leading to quick increase in strains and curvature there. This curvature is not representative for the entire beam, and therefore application of Eq. (5) would lead to an overestimation of deflection. Therefore, in this paper, Eq. (5) is used up to the bending moment $M_{\varepsilon u}$ when UHPFRC in the bottommost layer reaches ε_u. Beyond this point, the moment–deflection curve is linearly extrapolated up to M_{Rd}. The ultimate bending moment M_{Rd} is found numerically using the layered model and respecting ε_u of both UHPFRC and reinforcement bar.

At stage III, the beam which was previously loaded such that $M_{max} > M_{El}$ is unloaded until the bending moment is equal to the lower bending moment M_{min}. Within the distance ξ from the support, the beam remains elastic, and $\phi_1 = \phi(M_\xi)$, where $M_\xi = M_{min} \cdot \frac{\xi}{a}$. Respectively, $\phi_2 = \phi(M_{min})$. Equation 5 can be used to calculate the mid-span deflection only if the curvature distribution presented in Fig. 5 is respected. Since the stiffness along the beam between ϕ_1 and ϕ_2 depends on the strain and stress distribution attained at M_{max} in each section, the curvature distribution is investigated analytically in this paper, in Sect. 5.1.2.

5 Results
5.1 Type I Beams
The experimental results, as well as the procedure and results of calculation of deflection, are first explained in detail for beams of type I, with rebar diameter Ø20 mm, and spacing of load application points of $b = 0.7$ m. Two beams were tested until failure. Bi-linear elastic-strain hardening material model was used of UHPFRC, and elastic–plastic material model was used for steel reinforcement bar, as described previously.

5.1.1 Beam Deflection due to Monotonic Loading

The envelope moment–deflection curve obtained from testing until failure of the beams is presented in Fig. 6. Two methods were used for calculation of deflection: (1) constant stiffness along the beam using the curvature in the constant bending moment zone (formula 4 for all loading stages), and (2) bi-linear moment–curvature method as described previously. The difference between the two methods is marginal, due to the relatively large spacing of the load application points $b = 0.7$, explaining negligible influence of the relatively small elastic portions of the beam.

Despite that the two tested beams were virtually identical in terms of boundary conditions, dimensions and material, their stiffnesses differ considerably. The deflection of one beam at ultimate resistance is 12% larger than of the other. This can be attributed to the scatter of properties of UHPFRC (Oesterlee et al., 2009). However, the ultimate bending resistance is almost identical. Importantly, good agreement between model and experimental results were found.

The stress and strain distributions during multiple load steps in the critical section are presented in Fig. 7 together with the bending moment, mid-span deflection, stress in rebar and beam curvature. The calculation method was verified against strain gauges glued on rebars in Sawicki et al. (2022). Fig. 8 presents the obtained bending moment–curvature relationship in the critical section, with M_{El} and M_y values marked, where M_y indicates yielding of reinforcement and thus loss of bi-linearity which often occurs close to M_{Rd}. The transition from elastic to strain hardening is gradual. It takes place between the loading under which the response of cross-section is fully elastic ($M_{El} = 12.7$kNm, see Fig. 7a) and the bending moment of around 30kNm, when the zone of UHP-FRC stretches over around 200 mm from the bottom of the beam (Fig. 7b). The second change of linearity occurs at yielding of the reinforcement bar (Fig. 7e). It can be therefore concluded that the bi-linearity assumption of bending moment–curvature relationship holds until the reinforcement bar reaches its yielding strength. In Fig. 6 no change of curvature is visible around $M_{\varepsilon u}$ for the modelling results due to linear extrapolation of deflection as mentioned previously. For experimental results however, gradual softening of the deflection curve can be observed as the critical section weakens and a hinge is formed. The rapid softening is evident for the calculated curvature in the critical section presented in Fig. 8, reflecting the behavior of the tested beams.

The calculated deflection follows well the experimental results up to 75% of M_{Rd}, at which stage the strain in rebar is about 2.5‰, as presented in Fig. 7d. Beyond this
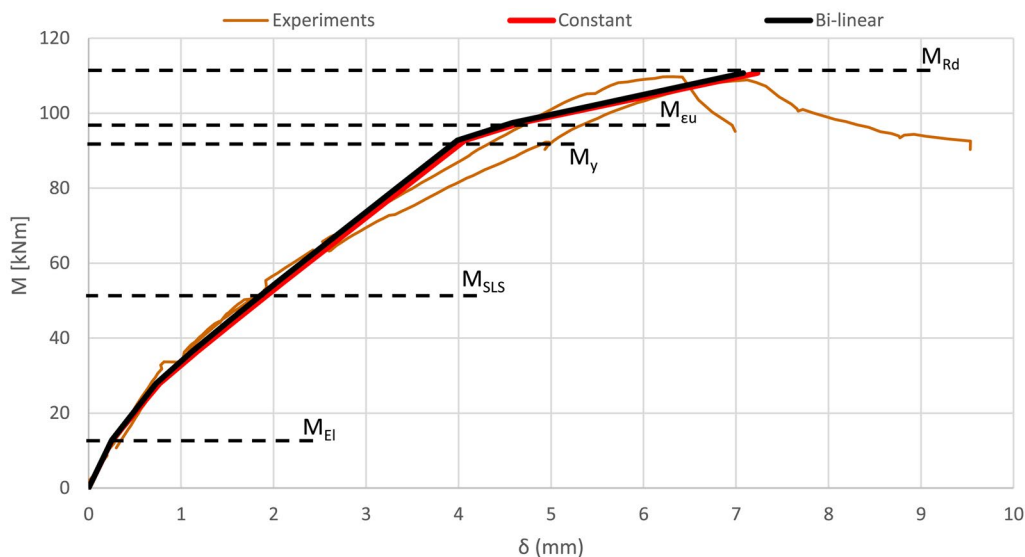

Fig. 6 Type I beams with b = 0.7 m: moment–deflection plots under monotonic loading with calculated elastic (M_{EL}), rebar yielding ($M_y = M_{II}$), ultimate bending resistance (M_{Rd}) and Serviceablity Limit State (M_{SLS}) assumed at 50% bending moments

(See figure on next page.)

Fig. 7 Calculated theoretical stress and strain profiles at monotonic loading of beams Type 1, b = 0.7 m; M—bending moment, δ—deflection at mid-span, σ$_s$—stress in rebar, φ—curvature in the critical section of bending moment zone

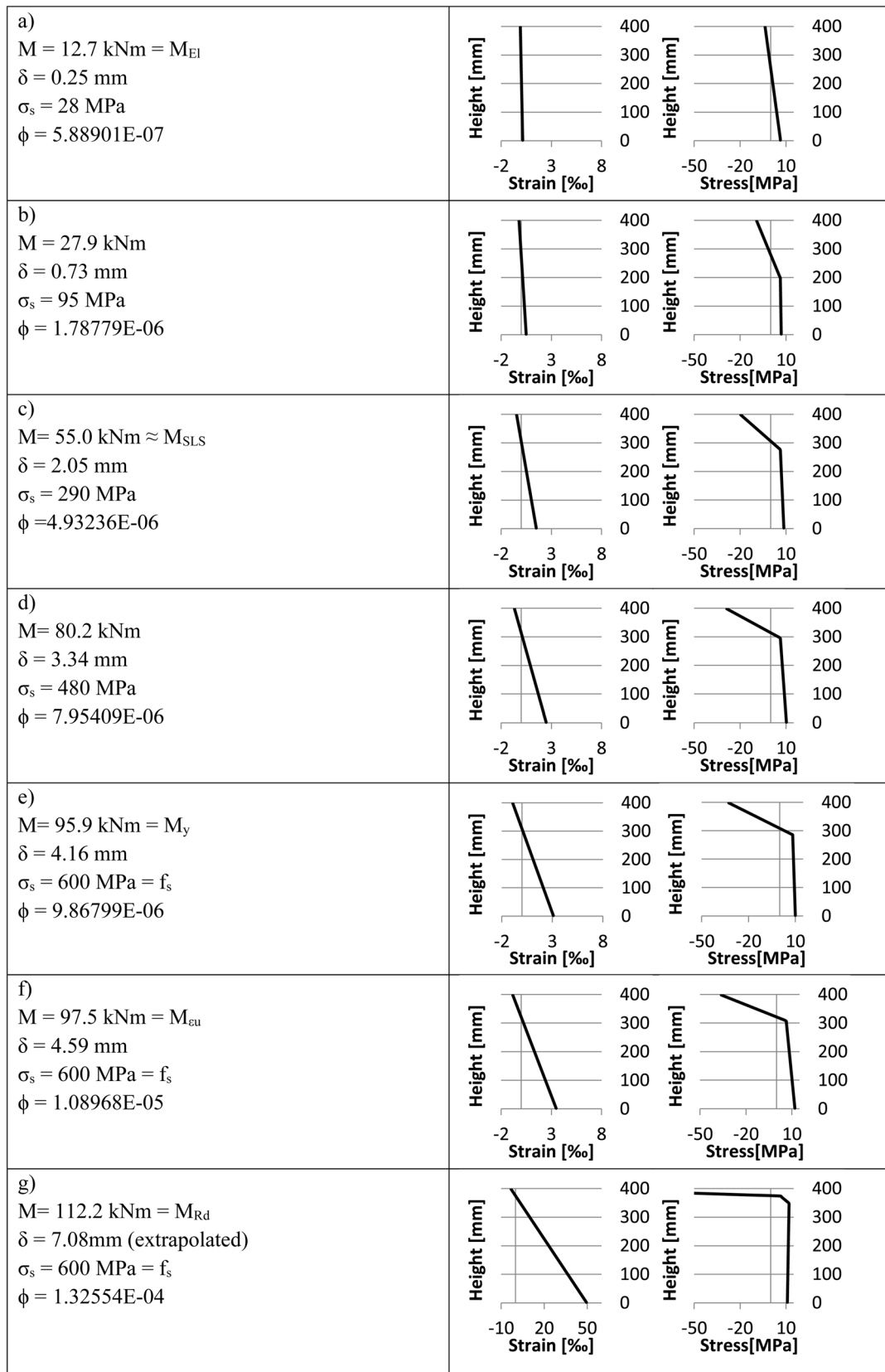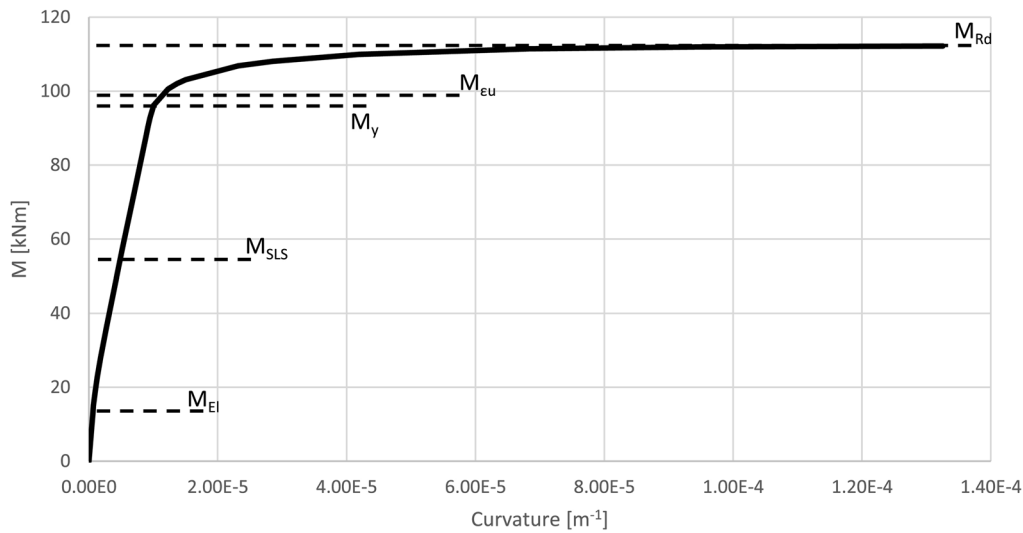|	
a) $M = 12.7$ kNm $= M_{El}$ $\delta = 0.25$ mm $\sigma_s = 28$ MPa $\phi = 5.88901E\text{-}07$	
b) $M = 27.9$ kNm $\delta = 0.73$ mm $\sigma_s = 95$ MPa $\phi = 1.78779E\text{-}06$	
c) $M = 55.0$ kNm $\approx M_{SLS}$ $\delta = 2.05$ mm $\sigma_s = 290$ MPa $\phi = 4.93236E\text{-}06$	
d) $M = 80.2$ kNm $\delta = 3.34$ mm $\sigma_s = 480$ MPa $\phi = 7.95409E\text{-}06$	
e) $M = 95.9$ kNm $= M_y$ $\delta = 4.16$ mm $\sigma_s = 600$ MPa $= f_s$ $\phi = 9.86799E\text{-}06$	
f) $M = 97.5$ kNm $= M_{\varepsilon u}$ $\delta = 4.59$ mm $\sigma_s = 600$ MPa $= f_s$ $\phi = 1.08968E\text{-}05$	
g) $M = 112.2$ kNm $= M_{Rd}$ $\delta = 7.08$mm (extrapolated) $\sigma_s = 600$ MPa $= f_s$ $\phi = 1.32554E\text{-}04$	

Fig. 7 (See legend on previous page.)

Fig. 8 Bending moment–curvature diagram at the critical cross-section of Type I beam
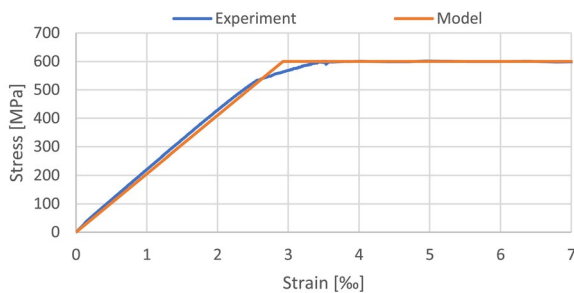

Fig. 9 Real and modeled response of steel rebar under tensile action, Type I rebar (Ø20 mm)

moment, the modelled beam is overly stiff. This comes from the loss of bi-linearity of the moment–curvature relationship due to the simplification of steel reinforcement constitutive behavior as elastic-perfectly plastic. The abrupt change between two regimes leads to higher stiffness than in reality showing a smooth transition up to the yielding, as presented in Fig. 9. This influences in particular the beam response when the rebar stress is higher than the nominal yield stress of 500 MPa, thus at bending moment higher than around 80 kNm. Consequently, this elastic-perfectly plastic material model for the steel rebar also causes an abrupt change of beam deflection once the rebar is yielding at the bending moment M_y.

After yielding of the rebar, the model presents a softer response up to M_ε, when part of the UHPFRC enters into the softening regime. From then on, the calculated curvature in the critical section is no more representative for the rest of the beam, and therefore the deflection is extrapolated linearly as mentioned before. Interestingly, it corresponds well with the experimental results up to

M_{Rd}. Noteworthy, the calculated M_{Rd} is almost identical with the experimental value, proving not only the correctness of the deflection model, but also the accuracy of the material model and representability of the results from material testing.

To quantify an error due to not taking into account the deflection caused by shear forces, this error was calculated at the peak load using the following equation (Pronk, 2007):

$$\delta_s = \frac{M(1 + \nu)}{a\alpha EHB} \cdot \frac{L}{2},\tag{6}$$

where ν is the Poisson ratio (assumed as 0.2), α is the shear correction coefficient depending on length and shape of beam (assumed as 0.85 (Pronk, 2007)), H and B are beam height and width respectively. B was taken here as the mean thickness of the rib of T-shaped beam. The calculated value $\delta_s = 0.05$ mm leads to error of 0.5%, which can be neglected.

5.1.2 Beam Curvature Under Loading–Unloading
The model for the calculation of deflection presented previously assumes a linear variation of curvature between ϕ_1 and ϕ_2. Due to the relatively complex constitutive law of UHPFRC, this assumption needs to be verified for beams under loading–unloading cycles. To do so, part of the beam between the elasticity limit cross-section ξ and the load application point a was divided into five sections, and for each cross-section the curvature was calculated separately using the strain and stress distributions as determined by Euler–Bernoulli theory and the previously discussed layered model. An exemplary curvature

distribution along half-beam (assuming symmetry) is presented in Fig. 10.

The subsequent curves represent the curvature along the beam when it is unloaded from the upper bending moment $M_{max}=M_y$ in multiple unloading steps to complete unloading at M_{min}. In all cases the curvature between ϕ_1 and ϕ_2 at ξ and a, respectively can be assumed as almost linear. This validates the hypothesis used for the calculation of beam deflection under loading–unloading.

5.1.3 Deflection Under Loading–Unloading

Fig. 11 presents the moment–deflection curves of the two beams under loading–unloading as obtained from testing as well as the values calculated using both the constant and bi-linear curvature methods. Residual deflection at unloading is clearly identifiable for both beams. For
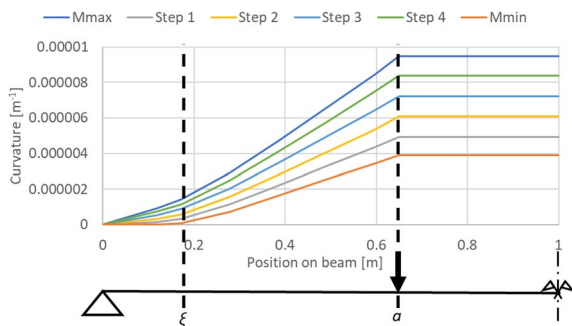

Fig. 10 Curvature along the beam of Type I b = 0.7 m during-unloading (one-half) at different unloading steps, with scheme of the beam

example, one of the beams unloaded from 93% of M_{Rd} (103 kNm) and a deflection of 5.4 mm, shows a residual deflection of 1.2 mm after unloading. This represents the possible overestimation by 20% of the beam relative deflection close to its ultimate resistance when the material behavior of UHPFRC under loading–unloading is not considered. On the other hand, after loading–unloading cycle the absolute total deflection for a given moment (e.g. M_{SLS}) is larger than before the pre-loading (57% for M_{SLS}). Clearly, the use of the elastic method would not yield correct results in the calculation of deflection.

The two analytical models yield similar results. Both of them overestimate the residual deflection, especially just before the ultimate bending resistance is reached. Since both models show similar results and the assumption of linearity of curvature was previously confirmed, the error can be attributed to the material model of UHPFRC. This indicates the importance of characterizing the behavior of UHPFRC under loading–unloading, which was not done previously according to the authors' knowledge.

Stress and strain profiles of UHPFRC in the constant bending moment zone are presented in Fig. 12. After pre-loading, when part of UHPFRC in the cross-section entered into the strain-hardening regime (Fig. 12a), distributed discontinuities of cementitious matrix appear. When the beam is unloaded (Fig. 12b), some part of UHPFRC enters into compression due to the strain being below the residual strain ($\varepsilon < \varepsilon_{res}$, see Fig. 2). Thanks to the perfect bond between rebar and UHPFRC, the reinforcement remains in tension. When the beam is again reloaded (Fig. 12c) and then unloaded such that the same strain ε_b is attained at
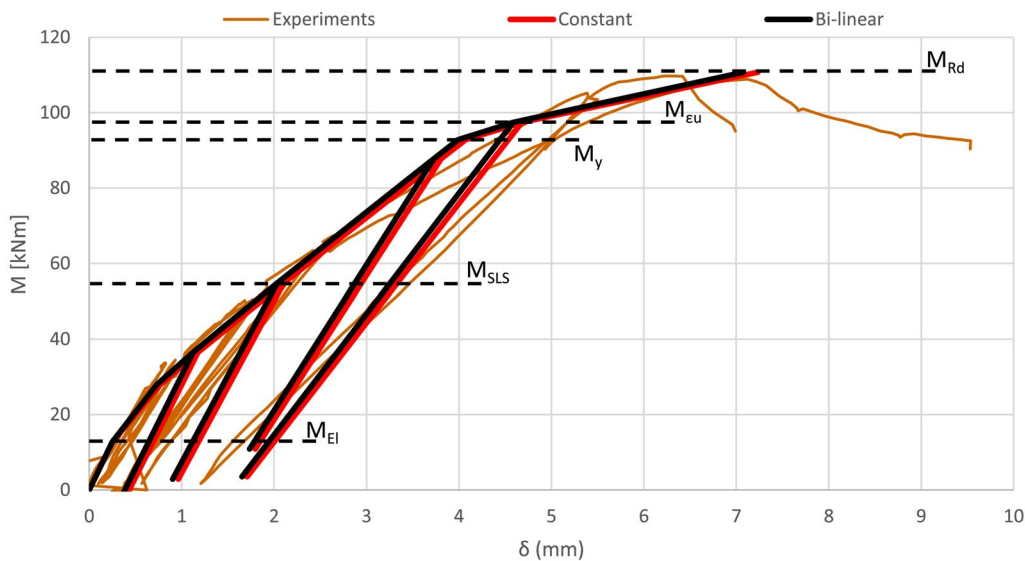

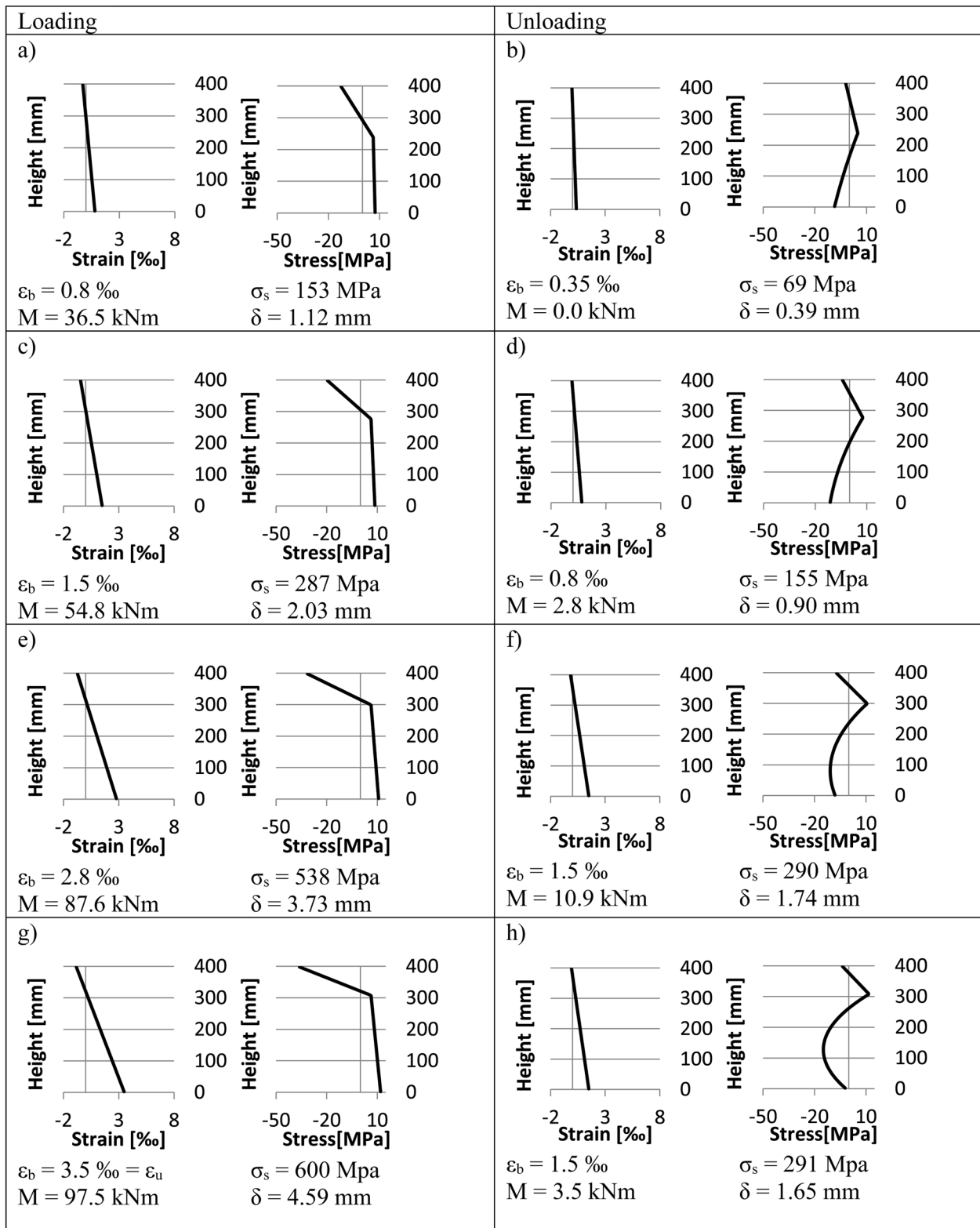**Fig. 11** Type I beams b = 0.7 m: moment–deflection plots under loading–unloading

Loading	Unloading
a)	**b)**
ε_b = 0.8 ‰ $\qquad$ σ_s = 153 MPa M = 36.5 kNm $\qquad$ δ = 1.12 mm	ε_b = 0.35 ‰ $\qquad$ σ_s = 69 Mpa M = 0.0 kNm $\qquad$ δ = 0.39 mm
c)	**d)**
ε_b = 1.5 ‰ $\qquad$ σ_s = 287 Mpa M = 54.8 kNm $\qquad$ δ = 2.03 mm	ε_b = 0.8 ‰ $\qquad$ σ_s = 155 Mpa M = 2.8 kNm $\qquad$ δ = 0.90 mm
e)	**f)**
ε_b = 2.8 ‰ $\qquad$ σ_s = 538 Mpa M = 87.6 kNm $\qquad$ δ = 3.73 mm	ε_b = 1.5 ‰ $\qquad$ σ_s = 290 Mpa M = 10.9 kNm $\qquad$ δ = 1.74 mm
g)	**h)**
ε_b = 3.5 ‰ = ε_u $\qquad$ σ_s = 600 Mpa M = 97.5 kNm $\qquad$ δ = 4.59 mm	ε_b = 1.5 ‰ $\qquad$ σ_s = 291 Mpa M = 3.5 kNm $\qquad$ δ = 1.65 mm

Fig. 12 Calculated theoretical stress and strain profiles at loading–unloading of beams Type I, b = 0.7 m presented in Fig. 11; ε_b—strain at the bottom, M—bending moment, δ—deflection at mid-span, σ_s—stress in rebar

the bottom of the element (Fig. 12d) as in the previous load step (Fig. 12a), the resulting bending moment is smaller. This is because of the contribution of compressive stress in the bottom part of cross-section. At the same time, since part of the beam remains elastic, the global deflection δ is smaller under this smaller bending moment. Similar mechanism can be observed in Fig. 12c, f. These observations confirm the important influence of the residual strain on the global structural response of a beam, in particular on the stress distribution in the cross section.

The significance of the generated compressive stress field in the bottom of a bent beam on the calculated magnitudes of stress range in the reinforcement bar during cyclic loading under serviceability was discussed previously in Sawicki et al. (2022). It was also identified as an important parameter in fatigue damage propagation in UHPFRC (Sawicki et al. 2021) and fatigue resistance of R-UHPFRC members (Sawicki & Brühwiler, 2019).

For Type I beams with loading points spacing $b = 0.5$ m (Fig. 13), experimental and calculated curves are in good agreement up to M_{SLS}, after which point the model yields overly stiff results. The beams were not loaded until failure, and in none of the cases M_{max} did cause rebar yielding. The unloading slope is modelled almost perfectly at early stages of loading, up to about 40 kNm. Later, the foreseen unloading behavior is overly rigid, leading to overestimation of residual deflection, similar to the previously discussed beams.

5.2 Type II and Type III Beams

Moment-deflection curves for Type II and III beams are discussed here. Only results obtained using the bi-linear moment–curvature model are presented.

The results for Type II beams, with load spacing $b = 0.4$ m, is presented in Fig. 14. Both beams were loaded until the rebar started to yield. The structural response of the beams, including unloading, is properly modelled until a bending moment of about 110 kNm (M_{SLS}), when around half of the UHPFRC cross-section is in the strain hardening stage, and the stress in the rebar is around 200 MPa. From this point on, loss of beam stiffness is underestimated by the model, leading to 20% smaller deflection than measured at 150 kNm. One of the possible reasons is nonuniformity of UHPFRC along the height of the beam section due to variation of fiber content and orientation, but it cannot be confirmed unequivocally. Unloading and residual deflection are modelled reasonably well. For both tested beams, loading was stopped at the onset of rebar yielding. In general, the model presents an overly stiff response under loading, however with good agreement between experimental and calculated deflection at unloading.

Fig. 15 presents the experimental results for six beams Type III, with load spacing $b = 0.4$ m. For this type of beams the experimental results varied considerably, i.e., measured deflections due to M_{SLS} were in the range of 2.0 mm to 2.4 mm. The calculated deflection is in accordance with the more rigid response. The unloading response is modelled as overly rigid. In general, structural behavior of Type III beams is well modelled up to M_{SLS} despite the scatter of experimental results.
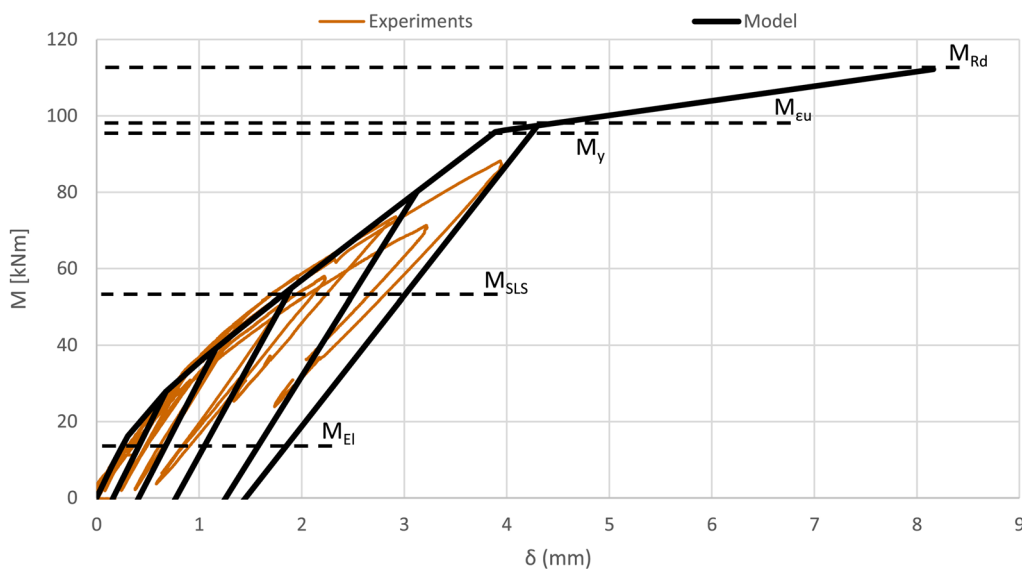

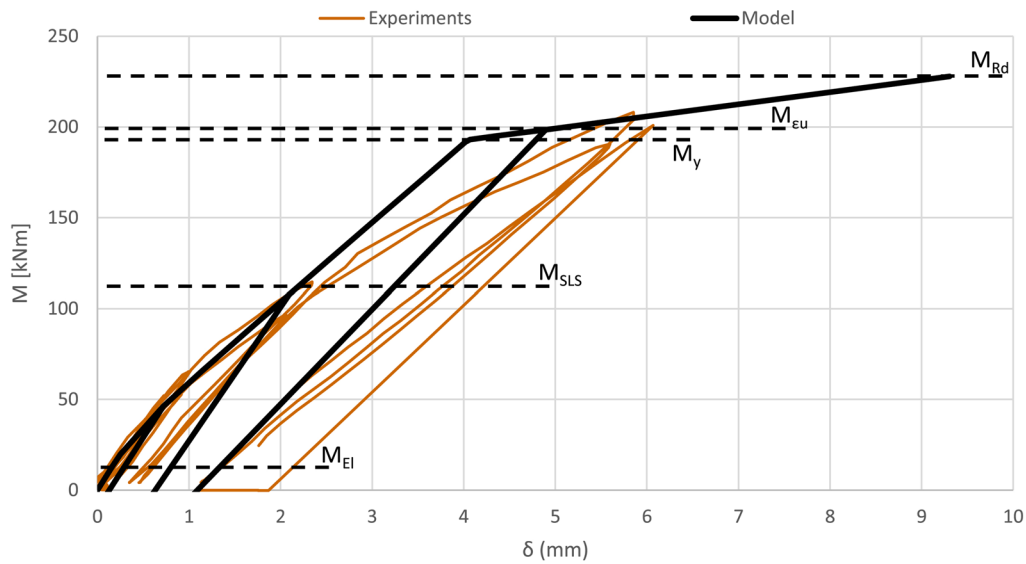**Fig. 13** Type I beams b = 0.5 m: moment–deflection plots under loading–unloading

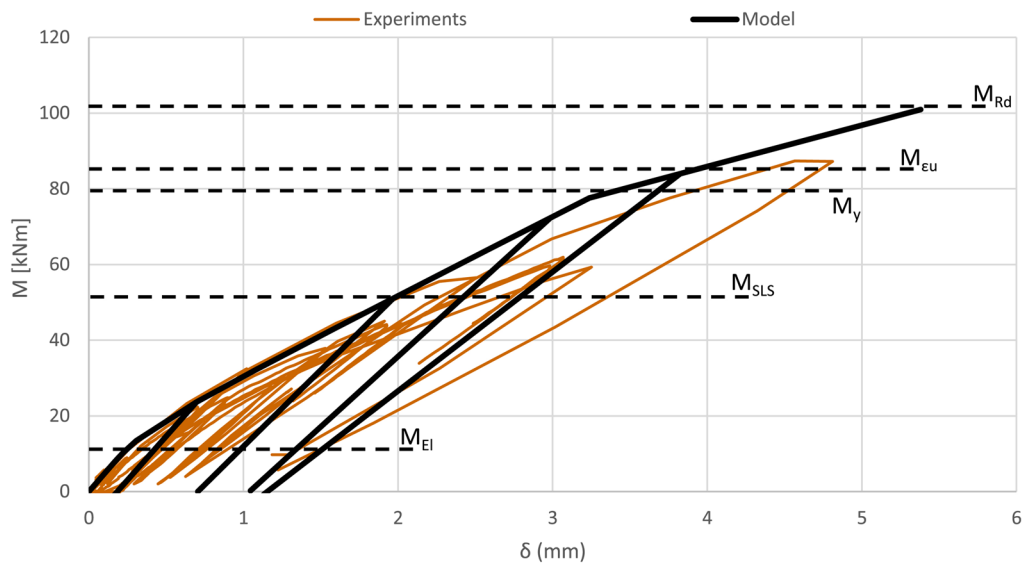**Fig. 14** Type II beams b = 0.4 m: moment–deflection plots under loading–unloading

Fig. 15 Type III beams b = 0.5 m: moment–deflection plots under loading–unloading

5.3 Discussion of Results

After analyzing the results of all experiments, two observations can be drawn: (1) the deflection of all beams under loading is underestimated between M_{SLS} and $M_{\varepsilon u}$, and calculated correctly otherwise; (2) the unloading path is modelled as overly rigid and the residual deflection is overestimated. The former can be attributed to simplified elastic-perfectly plastic reinforcement bar material model, as discussed previously (see Fig. 9). The latter most probably comes from incorrect assumption concerning unloading secant E_{Ui}, which cannot

be confirmed without separate experimental campaign focused on loading–unloading of UHPFRC. The two phenomena confirm importance of detailed material models for the precise results of modelling.

6 Conclusions

This paper discusses the loading–unloading behavior of reinforced UHPFRC beams in terms of bending moment-deflection curves. The importance of strain-hardening UHPFRC and its material behavior on the structural response of a beam, showing residual deflection after

unloading, is investigated using an analytical model for the calculation of the deflection under loading–unloading of the beam. The following conclusions can be drawn:

- Important residual deflection of R-UHPFRC beams after loading–unloading cycles has been identified. It manifests itself from an early stage of loading—as soon as part of UHPFRC enters into the strain-hardening regime. Residual deflection affects bending moment values as obtained under service conditions of the beam (at around half of the ultimate bending resistance).
- The observed phenomenon has significant implications in the design of structures due to the remaining residual deflection after unloading as well as due to the re-loading path being different from the original one.
- During unloading, the bending moment–curvature relation remains bi-linear. As a consequence, an analytical formula like the one proposed in this paper, can be used for calculation of deflection.
- The proposed material model for UHPFRC yields calculated results in accordance with test results, up to around half of bending resistance. Nevertheless, it yields more rigid response for higher loading.

Declarations

Competing interests
The authors declare that they have no competing interests.

References
ACI Committee 440. ACI PRC-440.1-15 Guide for the Design and Construction of Structural Concrete Reinforced with Fiber-Reinforced Polymer Bars. American Concrete Institute; 2015.

Azmee, N. M., & Shafiq, N. (2018e). Ultra-high performance concrete: From fundamental to applications. *Case Studies in Construction Materials, 9*, e00197. https://doi.org/10.1016/j.cscm.2018.e00197

Bertola N, Schiltz P, Denarié E, Brühwiler E. A review of the Use of UHPFRC in bridge rehabilitation and new construction in Switzerland. *Frontiers in Built Environment 2021*;7.

Brühwiler E. "Structural UHPFRC": Welcome to the post-concrete era ! International Interactive Symposium on Ultra-High Performance Concrete, vol. 1, Des Moines, Iowa, USA: Iowa State University Digital Press; 2016. https://doi.org/10.21838/uhpc.2016.key.

Brühwiler, E., Friedl, H., Rupp, C., & Escher, H. (2019). Bau einer Bahnbrücke aus bewehrtem UHFB. *Beton-Und Stahlbetonbau, 114*, 337–345. https://doi.org/10.1002/best.201900010

Denarié E, Sofia L, Brühwiler E. Characterization of the tensile response of strain hardening UHPFRC-Chillon viaducts. In: *Proceedings AFGC-ACI-fib-RILEM Int. Symposium on Ultra-High Performance Fibre-Reinforced Concrete*, UHPFRC 2017-Pro 106, Montpellier, France: RILEM publications S.A.R.L.; 2017, p. 242–50.

EC2. Eurocode 2: Design of concrete structures-Part 1–1: General rules and rules for buildings 2005.

Gao, D., Gu, Z., Tang, J., & Zhang, C. (2020). Fatigue performance and stress range modeling of SFRC beams with high-strength steel bars. *Engineering Structures, 216*, 110706. https://doi.org/10.1016/j.engstruct.2020.110706

Garcez, M. R., & Da Silva Filho, L. C. P. (2009). Analytical solution to simulate the behavior of reinforced concrete beams post-strengthened with FRP strips. *Revista IBRACON De Estruturas e Materiais, 2*, 222–243. https://doi.org/10.1590/S1983-41952009000300002

Graybeal, B., Brühwiler, E., Kim, B.-S., Toutlemonde, F., Voo, Y. L., & Zaghi, A. (2020). International perspective on UHPC in bridge engineering. *Journal of Bridge Engineering, 25*, 04020094. https://doi.org/10.1061/(ASCE)BE.1943-5592.0001630

Khorami, M., Navarro-Gregori, J., & Serna, P. (2021). Tensile behaviour of reinforced UHPFRC elements under serviceability conditions. *Materials and Structures, 54*, 43. https://doi.org/10.1617/s11527-021-01630-z

Makita, T., & Brühwiler, E. (2014). Tensile fatigue behaviour of ultra-high performance fibre reinforced concrete combined with steel rebars (R-UHPFRC). *International Journal of Fatigue, 59*, 145–152. https://doi.org/10.1016/j.ijfatigue.2013.09.004

MCS EPFL. UHPFRC Map Switzerland. Map of UHPFRC Applications in Switzerland 2023. https://www.epfl.ch/labs/mcs/mcs-laboratory-for-maintenance-and-safety-of-structures/uhpfrc-map-switzerland/. Accessed 23 May 2023.

Müller S, Mechtcherine V. Behaviour of strain-hardening cement-based composites (SHCC) under force-controlled cyclic loading. In: *Proceedings of the 9th International Conference on Fracture Mechanics of Concrete and Concrete Structures*, IA-FraMCoS; 2016. https://doi.org/10.21012/FC9.169.

Naaman AE. Fiber reinforced cement and concrete composites. 1st edition. Sarasota, Florida: Techno Press 3000; 2018.

Oesterlee C, Denarié E, Brühwiler E. Strength and deformability distribution in UHPFRC panels. In *Proceedings of 4th International Conference on Construction Materials: performance, innovations and structural implications*: ConMat '09: August 24(Mon.)-26(Wed.),2009, vol. 1+2, Nagoya Congress Center, Nagoya, Japan: 2009, p. 390–7.

Oesterlee C. Structural Response of Reinforced UHPFRC and RC Composite Members. École polytechnique fédérale de Lausanne, 2010.

Peng, F., Fang, Z., & Cui, S. (2022). Deflection calculation for reinforced ultra-high-performance concrete beams based on effective moment of inertia. *ACI Structural Journal, 119*, 263–275. https://doi.org/10.14359/51734523

Pronk AC. Theory of the Four Point Dynamic Bending Test – Part IV: Pure Bending & Shear De-formation. 1st European 4PB workshop, Delft, Netherlands: 2007, p. 24.

Sadaghian, H., Pourbaba, M., ZeinaliAndabili, S., & Mirmiran, A. (2021). Experimental and numerical study of flexural properties in UHPFRC beams with and without an initial notch. *Construction and Building Materials, 268*, 121196. https://doi.org/10.1016/j.conbuildmat.2020.121196

Sawicki B, Brühwiler E. Static behavior of reinforced UHPFRC beams with minimal cover thickness. In: *Proceedings of the 2IIS-UHPC-The 2nd International Interactive Symposium on Ultra-High Performance Concrete*, Albany, USA: 2019.

Sawicki B, Brühwiler E, Bassil A. Deformational behavior and damage mechanism of R-UHPFRC beam subjected to fatigue loading. Mater Struct 2021; Accepted.

Sawicki, B., & Brühwiler, E. (2021). Fatigue resistance of reinforced UHPFRC beams. *International Journal of Fatigue, 148*, 106216. https://doi.org/10.1016/j.ijfatigue.2021.106216

Sawicki, B., Brühwiler, E., & Denarié, E. (2022). Inverse analysis of R-UHPFRC beams to determine the flexural response under service loading and at ultimate resistance. *Journal of the Structural Engineering American Society of Civil Engineers, 148*, 04021260. https://doi.org/10.1061/(ASCE)ST.1943-541X.0003239

Shen, X., Brühwiler, E., & Peng, W. (2020). Biaxial flexural response of strain-hardening UHPFRC circular slab elements. *Construction and Building Materials, 255*, 119344. https://doi.org/10.1016/j.conbuildmat.2020.119344

Soranakom, C., & Mobasher, B. (2007). Closed-form solutions for flexural response of fiber-reinforced concrete beams. *Journal of Engineering Mechanics, 133*, 933–941. https://doi.org/10.1061/(ASCE)0733-9399(2007)133:8(933)

Visalvanich K, Naaman A. Compliance measured fracture toughness of mortar and fiber reinforced mortar. In: Freiman S, Fuller E, editors. Fracture mechanics for ceramics, rocks, and concrete, 100 Barr Harbor Drive, PO Box C700, West Conshohocken, PA 19428-2959: ASTM International; 1981, p. 141–56. https://doi.org/10.1520/STP28303S.

Wang X. Analytical load-deflection equations for beam and 2-D panel with a bilinear moment-curvature model. Master thesis. Arizona State University, 2015.

Wille K, Naaman AE. Fracture energy of UHP-FRC under direct tensile loading. In: Oh, B. H., et al. (eds) *Fracture mechanics of concrete and concrete structures—recent advances in fracture mechanics of concrete.* Seoul, Korea: Korea Concrete Institute; 2010.

Yang, I.-H., Joh, C., & Bui, T. Q. (2019). Estimating the tensile strength of ultra-high-performance fiber-reinforced concrete beams. *Advances in Materials Science and Engineering, 2019*, 16. https://doi.org/10.1155/2019/5128029

Yoo, D.-Y., Banthia, N., & Yoon, Y.-S. (2016). Predicting service deflection of ultra-high-performance fiber-reinforced concrete beams reinforced with GFRP bars. *Composites Part b Engineering, 99*, 381–397. https://doi.org/10.1016/j.compositesb.2016.06.013

Yoo, D.-Y., & Yoon, Y.-S. (2016). A review on structural behavior, design, and application of ultra-high-performance fiber-reinforced concrete. *International Journal of Concrete Structures and Materials, 10*, 125–142. https://doi.org/10.1007/s40069-016-0143-x

Publisher's Note

Bartłomiej Sawicki   Ex-doctoral researcher at MCS, EPFL under supervision of EB, currently post-doctoral researcher at ITE, TUBS.

Eugen Brühwiler   Professor and head of the Laboratory for Maintenance and Safety of Structures (MCS), EPFL.